



In Vivo Adaptive Optics Ophthalmoscopy Correlated with Histopathologic Results in Cancer-Associated Retinopathy

Zoë R. Williams, MD,¹ Ethan A. Rossi, PhD,^{2,3} David A. DiLoreto, Jr., MD, PhD^{1,4}

Purpose: To demonstrate the validity of adaptive optics scanning laser ophthalmoscopy (AOSLO) imaging of the retina in human disease based on clinicopathologic correlation in a patient with cancer-associated retinopathy (CAR).

Design: Case report.

Participant: Sixty-four-year-old man with CAR.

Methods: Fundus photography, electroretinography, visual field testing, fundus autofluorescent imaging, spectral-domain OCT scans, AOSLO, and histopathologic analysis were performed.

Main Outcome Measure: Comparison of AOSLO with histopathologic results.

Results: Changes in photoreceptor morphologic features were correlated highly between AOSLO and histopathologic results.

Conclusions: We present a unique case where a patient with a rare and fatal disease, CAR, underwent AOSLO imaging during the course of the disease, and then shortly thereafter, postmortem histopathologic analysis of the eyes was carried out. This is the first report of use of AOSLO to elucidate further the retinal changes that occur in CAR and the first study to demonstrate correlation of AOSLO with histopathologic results in any human disease. *Ophthalmology Retina* 2018;2:143-151 © 2017 by the American Academy of Ophthalmology

Cancer-associated retinopathy (CAR) is a paraneoplastic disorder in which tumor antigens induce the production of antibodies that cross-react with retina-specific antigens causing retinal degeneration and bilateral vision loss.¹⁻⁴ Malignancies causing paraneoplastic retinopathy include lung, hematologic, gynecologic (ovarian, endometrial, uterine, cervical), breast, prostate, bladder, colon, thymus, and melanoma.^{5,6} Early in the course of the disease, fundus-scopic changes can be minimal, leading to delay in diagnosis and treatment. Diagnosis of CAR also can be difficult because retinal disease resulting from CAR can precede the discovery of malignancy, and serum antiretinal antibodies are not always detected or, if present, are not specific for CAR.⁷ In addition to examination and standard imaging, assessment of patients suspected of having CAR includes malignancy screening, electroretinography to demonstrate decreased photoreceptor function, and serum testing to detect circulating antiretinal antibodies. Although there is no standardized treatment protocol, there have been numerous publications suggesting visual improvement with early immunosuppression.^{2,4,7,8}

The pathophysiologic features of CAR have not been elucidated fully, and not all antiretinal antibodies are pathogenic.^{1,3-5,7,8} There have been limited human histologic studies of CAR that have shown photoreceptor loss.^{9,10} More recent studies have focused on the use of OCT^{6,11-13} and fundus autofluorescence^{6,11,13} in identification of early retinal changes. Herein, we combined use of these conventional retinal imaging systems with adaptive optics scanning laser

ophthalmoscopy (AOSLO), which allows nearly diffraction-limited resolution and has been used to characterize numerous cell classes and a variety of ocular conditions at a microscopic scale in the living eye.¹⁴ However, there have been no studies that have been able to confirm that adaptive optic (AO) images correlate with histopathologic features in humans. We present a unique situation in which a patient with a rare and fatal disease, CAR, underwent AOSLO imaging at 2 time points during the course of disease, and then shortly thereafter, histopathologic postmortem analysis of the eyes was performed. This allowed us to use AO imaging to elucidate further the retinal changes that occur in CAR and, more importantly, to correlate AO imaging with histopathologic results for the first time in any human disease.

Methods

Clinical Presentation

A 64-year-old white man with hypertension, hyperlipidemia, and asthma sought treatment for painless, progressive bilateral vision loss over 1 month. He reported associated dimming of his vision, but noted in bright light that glare actually was intensified. He reported no systemic symptoms, including jaw claudication, scalp tenderness, headaches, arthritis, myalgias, recent weight loss, fevers, or chills. There was no family history of unexplained visual loss.

His medications included aspirin, sertraline, lisinopril—hydrochlorothiazide, tiotropium bromide, fluticasone—salmeterol, fish oil, and a multivitamin. His ocular medication included travoprost and brimonidine in both eyes for elevated intraocular pressure. He

was a former smoker with a 50-pack year history and reported no history of cancer. While alive, the patient gave consent for publication of his clinical study and adaptive optics results. His family gave consent to for post-mortem analysis of his eyes and publication of any papers that resulted from this.

His prior workup included normal magnetic resonance imaging results of the brain with and without gadolinium, normal erythrocyte sedimentation rate, normal C-reactive protein levels, and negative temporal artery biopsy results. On initial presentation, his best-corrected visual acuity was 20/100 in the right eye and hand movements at 6 inches in left eye. His pupils were sluggish with a trace left afferent pupillary defect. He was unable to identify any solid color pages with either eye. Intraocular pressure was 22 mmHg in the right eye and 20 mmHg in the left eye. Anterior segment examination revealed fine keratic precipitates. Dilated funduscopy examination demonstrated vitreitis and marked bilateral arteriolar attenuation (Fig 1).

On Goldmann visual field (GVF) testing, no isopters were identified using a size V4e target. Because of concern for CAR, he was treated with prednisone (80 mg orally per day) pending Ganzfeld electroretinography. Ganzfeld electroretinography showed markedly diminished results (Fig 2). Antiretinal autoantibody test results were positive for antibodies against 30-kDa (carbonic anhydrase II), 36-kDa (glyceraldehyde 3-phosphate dehydrogenase), 40-kDa (aldolase), 45-kDa (arrestin), and 62-kDa proteins, and immunohistochemistry analysis showed staining of the photoreceptor cell layer in human retina (Ocular Immunology Laboratory, Oregon Health & Science University, Portland, Oregon). Malignancy screening revealed a 2-cm right upper-lobe mass with paratracheal and subcarinal lymphadenopathy. Biopsy revealed poorly differentiated carcinoma with mixed small- and large-cell carcinoma components. He started combined chemotherapy and radiation.

His vision improved to 20/60 in the right eye, but worsened to no light perception in the left eye despite high-dose prednisone. He was able to identify 6/12 solid color pages with his right eye and had a 3° central island of vision on GVF. With attempted steroid taper, he demonstrated recurrent vision loss. He was treated by increasing his steroid dose and adding intravenous immunoglobulin and mycophenolate mofetil. Significant side effects developed with

mycophenolate and ultimately his vision and GVF results (Fig 3) in the right eye were stabilized with fluocinolone acetonide intravitreal implant (0.59-mg Retisert; Bausch and Lomb, Rochester, NY). Unfortunately, subsequent positron emission tomography computed tomography showed new liver metastases. His vision remained stable until his death 6 months after implantation.

Clinical Imaging

The patient underwent color fundus photography, confocal scanning laser ophthalmoscopy (cSLO), and spectral-domain (SD) OCT (Spectralis HRA+OCT; Heidelberg Engineering, Heidelberg, Germany). Confocal scanning laser ophthalmoscopy images were obtained using near infrared reflectance, blue light fundus autofluorescence (FAF; excitation, 488 nm), and near infrared FAF (excitation, 805 nm) imaging. High-density SD OCT scans were obtained of the central macula.

Adaptive Optics Scanning Light Ophthalmoscopy

Imaging was performed using an adaptive optics scanning laser ophthalmoscope nearly identical in design to one described in detail previously.¹⁵ Wavefront sensing was performed using an 847-nm laser diode, while imaging light was delivered simultaneously with a superluminescent diode with a center wavelength of 796 nm and full width at half maximum of 14 nm. The imaging field was approximately $1.5^\circ \times 1.5^\circ$; image sequences were obtained at a frame rate of approximately 20 Hz. Imaging was targeted using patient fixation; the fixation target, a large white circle, was viewed off of a laser window placed in front of the eye and was guided by a fundus image, as described elsewhere.¹⁶ Two AOSLO imaging sessions were completed. At the first imaging session, 4 months after the initial presentation, images were obtained of a central square region approximately $900 \times 900 \mu\text{m}$, centered on the fovea, and of strips that extended from the center of this area to approximately 2.5 mm nasal, 2.4 mm temporal, 2.4 mm superior, and 2 mm inferior. Strips of eccentric areas varied in width from approximately 400 to 1000 μm . During the second imaging

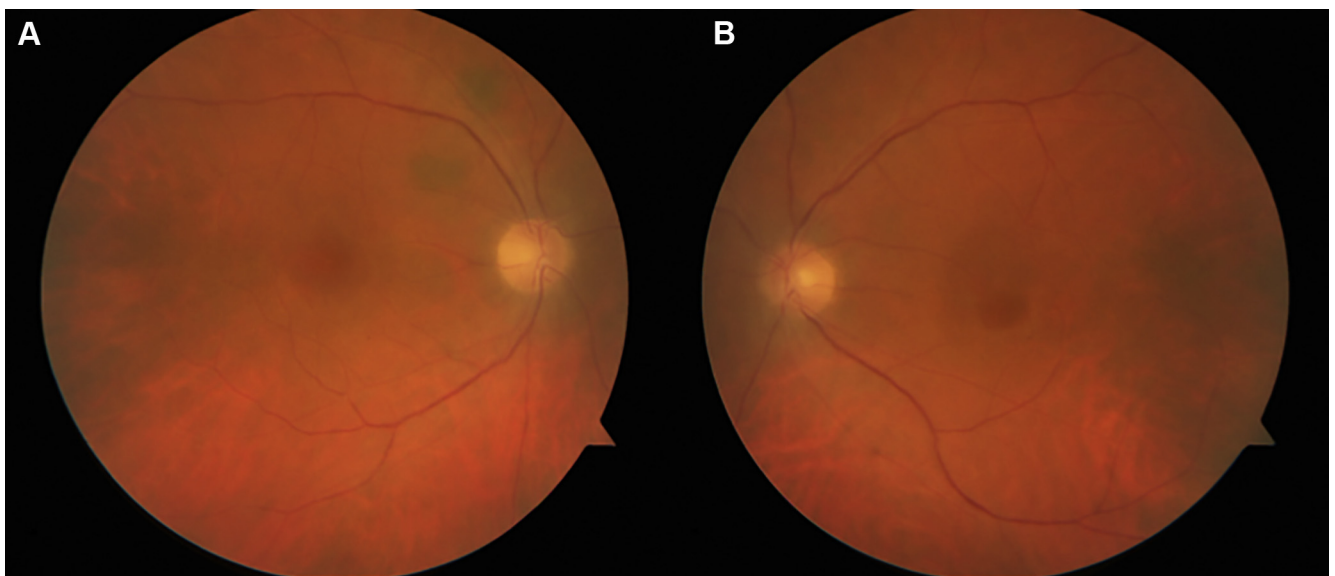


Figure 1. Fifty-degree color fundus photographs of (A) the right and (B) the left eyes. Both photographs show haze from vitreitis and severe arteriolar attenuation.

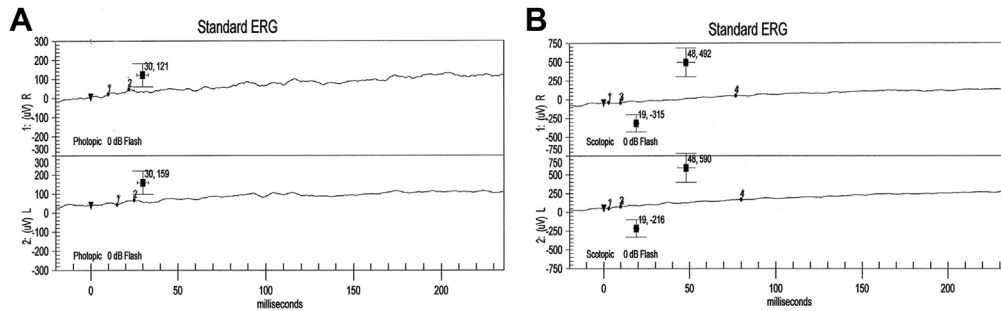


Figure 2. Ganzfeld full-field electroretinography (ERG) results showing markedly diminished (A) photopic and (B) scotopic responses bilaterally.

session 4 weeks later, images were acquired of a square region approximately 1.3×1.3 mm centered on the fovea.

Adaptive Optics Scanning Light Ophthalmoscopy Image Processing and Analysis

Adaptive optics scanning light ophthalmoscopy image sequences were registered and averaged using software described elsewhere,¹⁷ and averaged images were stitched together manually into montages using Adobe Photoshop (Adobe Systems, Inc, San Jose, CA). The size of features in AOSLO images were determined by scaling the axial length, measured with an IOLMaster (Carl Zeiss Meditec, Jena, Germany), to a Gullstrand no. 2 simplified relaxed schematic eye model. Adaptive optics images were overlaid on fundus photographs and cSLO FAF images that were scaled to the size of the AOSLO montages in Photoshop. En face cSLO images were overlaid to determine the precise location of SD OCT B-scans with respect to the AO images. Cone positions were identified using a semiautomated method; candidate cone positions were identified using an algorithm¹⁸ and then were corrected manually. Cone positions were

determined from images obtained at the second imaging session for 5 areas: a 200×200 - μm square centered on the foveola and 4 100×100 - μm areas located $300 \mu\text{m}$ eccentric to the center of the foveola in the nasal, temporal, superior, and inferior directions. Because most of the cone-like structures in the eccentric regions exhibited atypical structure compared with a normal age-matched control, a rather liberal criterion was established for manual correction of cone positions: all bright circular or elliptical features were marked as candidate cones. Cone statistics were calculated from cone positions using methods described in detail elsewhere.¹⁹

Histopathologic Analysis

Serial $6\text{-}\mu\text{m}$ paraffin sections of the formalin-fixed globe were obtained and stained with hematoxylin–eosin. Sections centered on the fovea were compared with AOSLO images in the same area.

Literature Search

PubMed was searched for combinations of the following key words for human studies: (1) *adaptive optics* and (*retinopathy* or *retinal degeneration* or [*retina* and *disease*]); and (2) *adaptive optics* and *retina* and (*pathology* or *histology* or *histopathology*). No other reports were found on AO imaging of CAR nor on AO imaging of the retina with correlation to histopathologic results in human disease.

Results

Spectral-Domain OCT

Spectral-domain OCT showed diffuse thinning with loss of the outer retinal layers in the extrafoveal areas and relative sparing in the foveal region with trace residual ellipsoid region remaining (Fig 4). Three months after presentation, SD OCT showed extensive thinning throughout the retina (Fig 5). Central subfield thickness was $152 \mu\text{m}$ in the right eye. Hyperreflective debris was seen at the level of the retinal pigment epithelium (RPE). It spared the subfoveal area and correlated with areas containing melanophages on histopathologic analysis. A faint remnant of the ellipsoid region could be detected. This correlated with the remaining outer nuclear layer nuclei and inner segments seen on histopathologic analysis.

Confocal Scanning Laser Ophthalmoscopy

Fundus images obtained using cSLO in FAF imaging mode exhibited an abnormal pattern. An irregularly shaped, roughly elliptical region of hypoautofluorescence was observed in the central

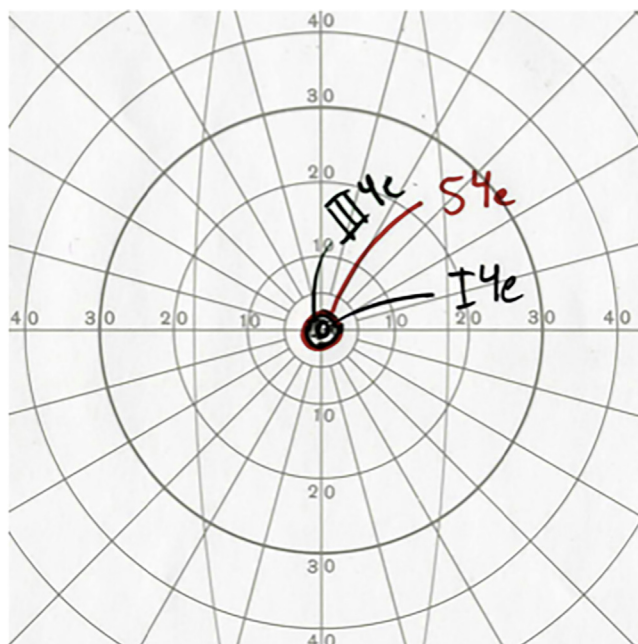


Figure 3. Goldmann perimetry showing a 3° central island of vision to the size V4e target in the right eye.

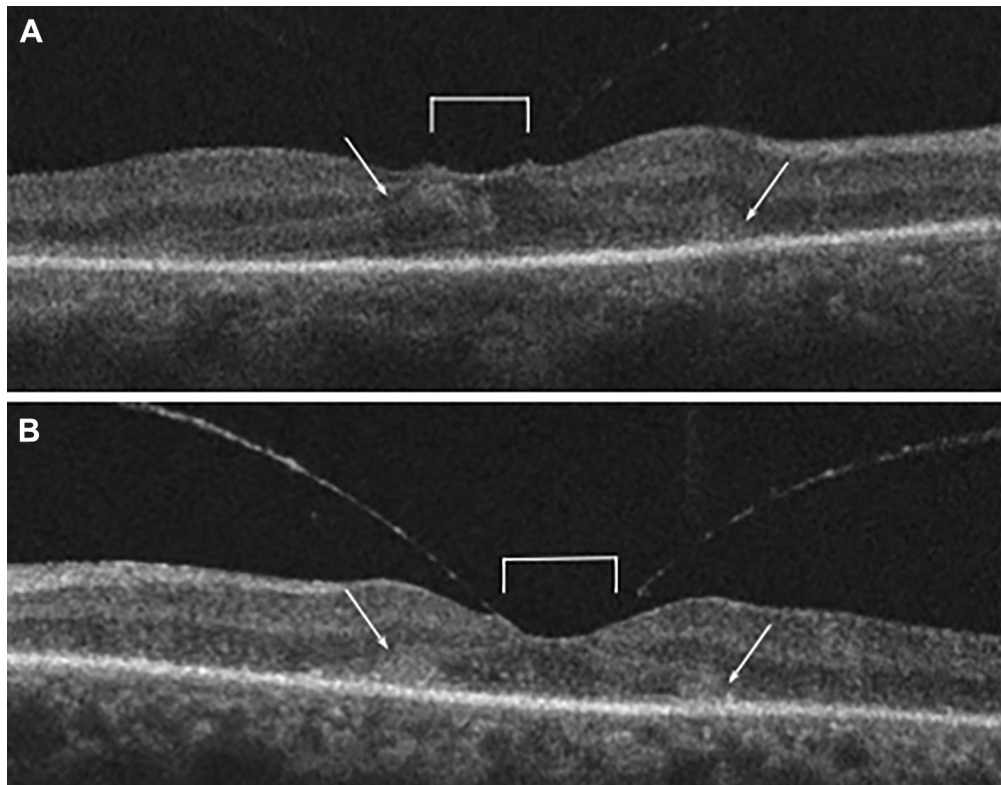


Figure 4. Spectral-domain OCT images obtained at presentation showing bilateral thinning with vitreomacular adhesions (brackets). Central subfield thickness is (A) 195 μm in the right eye and (B) 178 μm in the left eye. A, The right eye shows disorganization of the outer plexiform layer (OPL) and outer nuclear layer (ONL; arrows). The outer limiting membrane and ellipsoid region are difficult to identify. B, The left eye shows similar but more severe changes, with disorganized OPL and ONL in the subfoveal region (arrows).

macula with blue-light FAF (Fig 5A). The shape and appearance of this area was distinct from the central hypoautofluorescence of blue-light FAF typically observed in the central macula of normal eyes. This abnormal FAF pattern was approximately 1.6 mm in diameter along the horizontal meridian and approximately 1.3 mm in diameter along the vertical meridian. The margin of this area was hypoautofluorescent. The thickness of the margin varied from approximately 200 to 600 μm . The surrounding retinal area exhibited a mottled heterogeneous appearance that lacked the relative uniformity of FAF seen in normal retinas.

Adaptive Optics Scanning Light Ophthalmoscopy

Relatively normal-appearing cone photoreceptors were observed in a small, approximately elliptical area within the foveola (Fig 6B and C); this area spanned approximately 180 μm horizontally and approximately 130 μm vertically. A narrow band of hyporeflectivity approximately 20 to 30 μm wide containing sparse cones separated this central elliptical region from a surrounding annular area that contained a mix of both normal- and abnormal-appearing cones (Fig 6B, C, and 7A). This area also was approximately elliptical, with a horizontal diameter of 900 μm and a vertical diameter of 950 μm . Cone spacing in the fovea appeared to fall within the normal range (Fig 8), but was near the larger end of the range for aging eyes, with a minimum intercone distance of approximately 4 μm averaged over the central 100 \times 100 μm (Fig 7A). Peak cone density was

73 000 cones/ mm^2 ; this is lower than the lowest peak density reported by Curcio et al²⁰ and compared with normal variation based on retinal eccentricity and age as reported by Song et al²¹ in Figure 8. The reflectance of foveolar cones was somewhat irregular (Fig 7A). Cone structure at 300 μm was extremely abnormal, with large areas of cones that were hyporeflective interspersed with hyperreflective cones that exhibited irregular morphologic features (Fig 6B and C and Fig 7B, C, E, and F). The area outside the central hyperreflective cone containing region was relatively hyporeflective (Fig 7A) and exhibited very few structures that could be identified unambiguously as cones. This area appeared to contain clumps of hyperreflective material, including some that extended into the inner retina (Fig 9).

Histopathologic Analysis

The right eye retinal degenerative process was correlated to SD OCT images and AOSLO images based on the approximation to the foveal center found on serial sectioning. Diffuse loss of photoreceptors was seen with relative sparing in the foveal region (Fig 10), which correlated well with the SD OCT images. The remaining photoreceptor cells seemed to be cones based on their presence in the foveal region, nuclear chromatin pattern based on hematoxylin–eosin staining, and wide inner segments (Fig 10C). The outer nuclear layer in the foveal area was only 1 cell thick at this point in the disease process. This correlated well with the AOSLO images (Fig 7), which detail the decreased density of the photoreceptors compared with normal

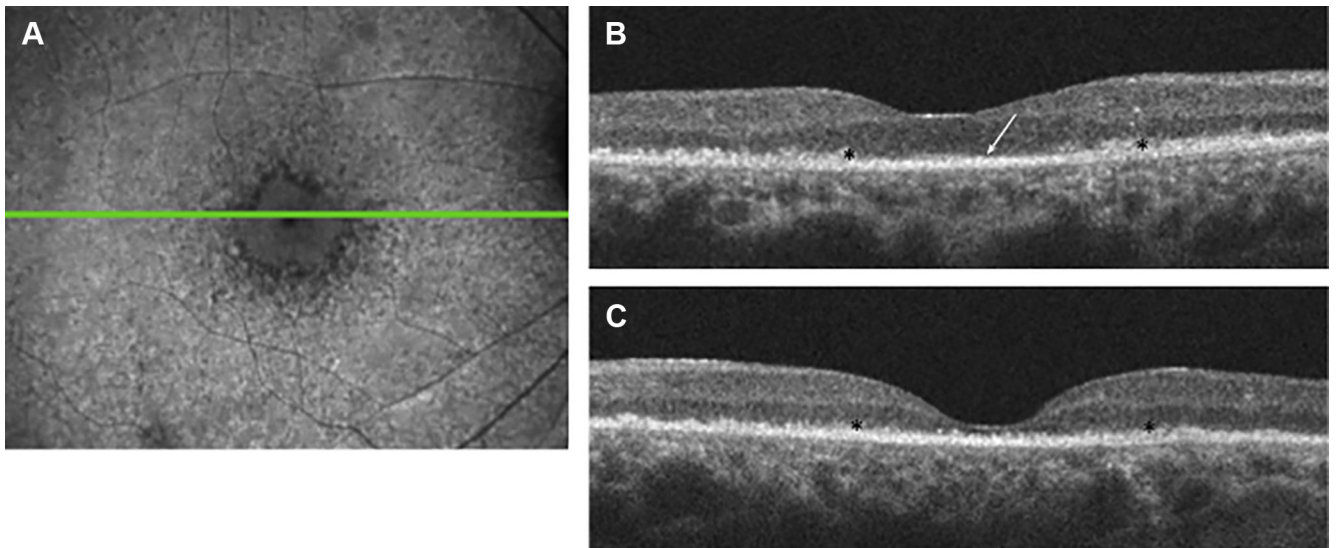


Figure 5. A, Fundus autofluorescence photograph (488 nm) obtained 5 months after presentation showing decreased hyperfluorescence in a well-circumscribed area around the fovea. The area of hyperfluorescence corresponds to the diffuse thinning and debris accumulation seen on OCT, and the hypo-fluorescent area of the central fovea correlates to the relative sparing of the outer retina, as seen on (B) spectral-domain (SD) OCT. B, C, Spectral-domain OCT scans obtained 3 months after presentation. The central subfield thickness was (B) 152 μm in the right eye and (C) 40 μm in the left eye. The level of the SD OCT slice shown for (B) the right eye corresponds to the green line in (A). Hyperreflective debris (asterisks) is seen above the retinal pigment epithelium in both eyes. It spares the subfoveal area of (B) the right eye, but includes the subfoveal area (C) in the left eye. No definitive outer plexiform layer or outer nuclear layer can be seen in the subfoveal area at this time in the right eye. There is complete foveal atrophy in the left eye. A faint remnant of the inner segment junction can just be detected (arrow). This correlates with the remaining photoreceptor cell nuclei and inner segments seen on histopathologic sections.

controls, as well as the increased apparent diameter of the cone inner segments compared with controls. As eccentricity from the foveal center increased, so did photoreceptor loss. Adaptive optics scanning light ophthalmoscopy demonstrated the same findings. Hyperreflective material documented in AOSLO (Fig 9) most likely represented melanophages, because this is what was seen on histopathologic examination at the edge of

the photoreceptor cell degeneration (Fig 10D). This hyperreflective material spared the subfoveal area and correlated well with the hyperreflectivity seen on SD OCT as well as the melanophages seen on histopathologic examination. The faint remnant of the ellipsoid region on SD OCT (Fig 5B) correlated with the remaining outer nuclear layer nuclei and inner segments seen on histopathologic sections (Fig 10C).

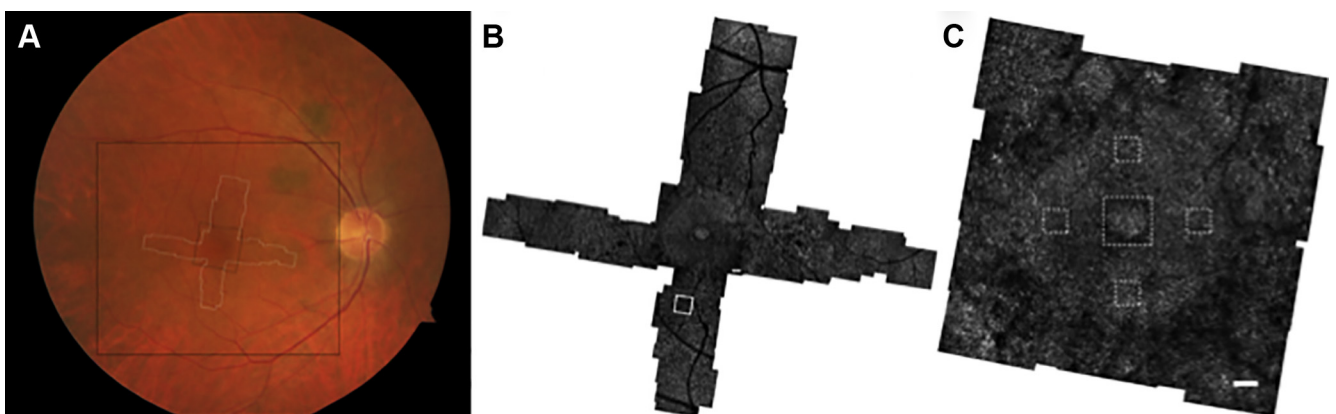


Figure 6. A, Fundus photograph of the right eye at presentation. White dashed line denotes area imaged with adaptive optics scanning laser ophthalmoscopy (AOSLO) at the first imaging session in (B). Black dashed line denotes area imaged with AOSLO on follow-up session in (C). Large solid black rectangle shows the area of the Spectralis confocal scanning laser ophthalmoscopy blue-light fundus autofluorescence shown in Figure 5. Adaptive optics montages obtained at (B) the initial and (C) follow-up imaging session 4 weeks later. Cone photoreceptors were visible in an approximately elliptical hyporeflective area approximately 900 μm in diameter centered on the fovea; this location appeared similar in each imaging session. Outside this area, cone-like structures were rare. Solid white square in (B) denotes the location of the through-focus images shown in Figure 9. Dashed white squares in (C) denote the areas shown in Figure 7. Scale bars are 100 μm .

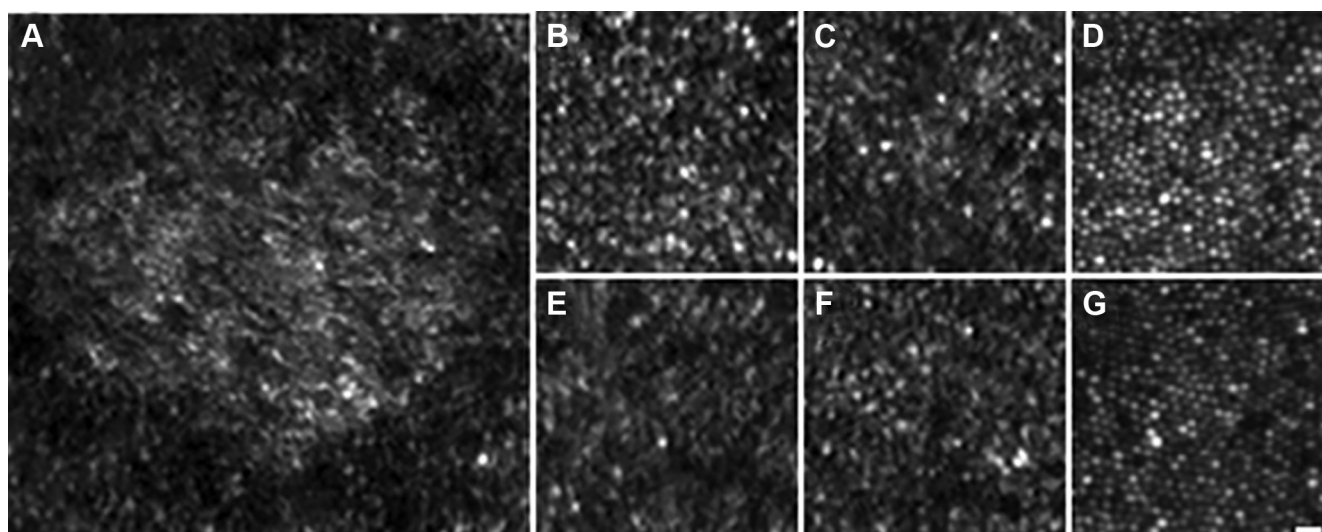


Figure 7. Adaptive optics scanning laser ophthalmoscopy images showing (A) an intact mosaic of foveal cones in the foveola. However, just outside the foveola, the cones showed (B, C, E, F) an abnormal appearance when compared with (D, G) images from a normal control. B–G, Images obtained from an eccentricity of 300 μm : (B) inferior, (C, D) superior, (E) temporal, and (F, G) nasal to the foveal center. Scale bar is 10 μm .

Discussion

Vision loss in CAR frequently occurs without visible evidence of retinal inflammation, suggesting a large pathogenic role for humoral immunity.²² Animal studies have shown that antiretinal autoantibodies, specifically antirecoverin antibodies, enter photoreceptor cells and trigger apoptosis, leading to retinal degeneration.^{22,23} In Lewis rats injected intravitreally with monoclonal antibody to recoverin, electron microscopy revealed vacuolization and apoptotic change in rod outer segments within 24 hours.²² It has been demonstrated that the presence of multiple antiretinal antibodies increases the risk of development of vision loss.²⁴ Our patient's serologic results were positive for 4 antiretinal autoantibodies (against carbonic anhydrase II, glyceraldehyde 3-phosphate dehydrogenase, aldolase, and arrestin) and 1 anti-optic nerve autoantibody (against 62-kDa protein).²⁵ In patients with either paraneoplastic or nonparaneoplastic autoimmune retinopathy, the presence of other antiretinal antibodies with anti-carbonic anhydrase II autoantibodies significantly increases the risk of vision loss consistent with additive effects.²⁴ Furthermore, Adamus et al²⁵ showed that anti-optic nerve autoantibodies are detected in more than half of patients with either nonparaneoplastic autoimmune retinopathy or CAR.

Glyceraldehyde 3-phosphate dehydrogenase is concentrated highly in rod outer segments⁷ and is known to be involved in cell metabolism, signaling, and synaptic transmission.^{7,25} Adamus and Karren²⁶ demonstrated that anti-carbonic anhydrase II autoantibodies induce retinal cell destruction via metabolic disruption (reducing intracellular pH and increasing intracellular calcium), which may trigger caspase activation. Wistrand et al²⁷ studied the distribution of carbonic anhydrase II in human donor eyes using immunocytochemistry and found high levels of staining in Müller cells (cytoplasm

and membranes) with variable staining in RPE (membranes). On histochemical studies, there was staining in the portion of some cones extending to the pigmented epithelium, in addition to the mitochondrial portion (heavily stained), cristae, and outer membranes of the cones, but no staining of rods.²⁷ The pathogenicity of our patient's other antiretinal antibodies have been less well studied. The pathogenesis has not been elucidated fully for many autoantibodies that also are seen in the serum of normal controls.^{7,11,25,28}

Prior histologic studies of CAR have shown destruction of the photoreceptor cell layer^{9,10} associated with melanophagic activity.¹⁰ In a histopathologic study published in 1993 by Adamus et al,⁹ full destruction of the photoreceptor cell layer in a patient with complete loss of vision resulting from CAR was reported. Sawyer et al¹⁰ described 3 patients with anaplastic tumors in whom histologic analysis showed significant photoreceptor degeneration, loss of the outer nuclear layer, and increased melanophages in the outer retina. Our patient maintained vision in the right eye until his death. Histopathologic sections of the right eye revealed complete loss of photoreceptor cell nuclei except at the fovea, where a single layer of nuclei was seen in the outer nuclear layer with attached cone inner segments. Although difficult to quantify, the inner segments of the remaining photoreceptors in some cases appeared irregular or shortened. This may account for the irregular appearance of the photoreceptors seen in the AO images, particularly near the margin of the preserved region.

Prior SD OCT and FAF studies demonstrated early changes in the outer retina in autoimmune retinopathies.^{6,11} Fundus autofluorescence with short-wavelength excitation capitalizes on the fluorescence of lipofuscin that naturally accumulates in the RPE as a byproduct of the visual cycle,

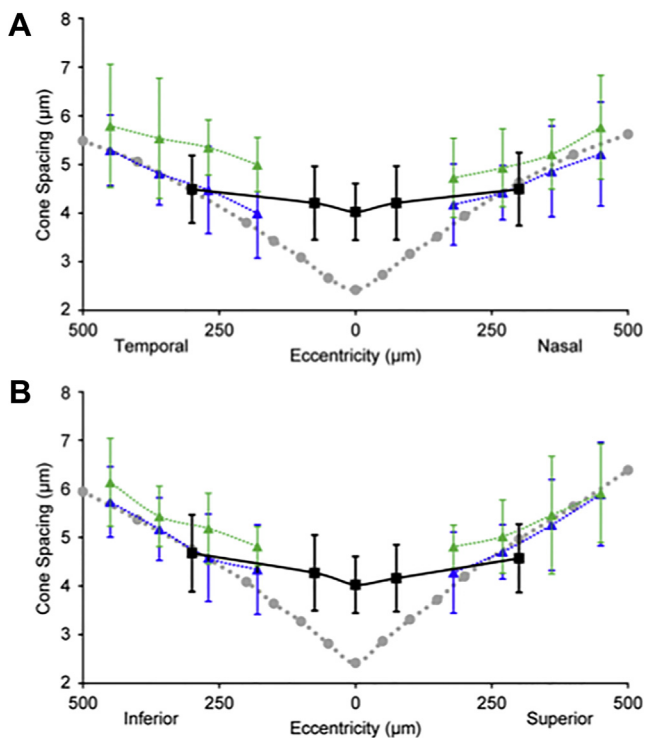


Figure 8. Graphs showing that foveal cone spacing seems to fall within normal limits despite the abnormal cone appearance. Measurements obtained for the cancer-associated retinopathy patient (black squares and lines) along the (A) horizontal and (B) vertical meridians are compared here with the mean of the measurements obtained from the histologic data of Curcio et al (gray circles and gray solid lines) and the in vivo adaptive optics data of Song et al for their young (blue triangles and lines) and old (green triangles and lines) groups. Measurements for the cones at the foveal center were obtained from a $100 \times 100\text{-}\mu\text{m}$ area centered on the image shown in Figure 7A. Measurements shown at $100 \mu\text{m}$ are from $100 \times 50\text{-}\mu\text{m}$ windows obtained from the margins of the image shown in Figure 7A. Measurements at $300 \mu\text{m}$ are from the images shown in Figure 7B, C, E, and F.

thereby indirectly assessing RPE damage.⁶ Lima et al^{6,13} hypothesized that the hyperautofluorescent ring seen in their 4 patients with autoimmune retinopathy (2 of whom had CAR) may represent increased levels of lipofuscin that precedes photoreceptor apoptosis similar to what has been described in retinitis pigmentosa. In all of their patients, SD OCT showed thinning of the outer nuclear layer, the ellipsoid region, and photoreceptor outer segment layer at the

inner border of the hyperautofluorescent ring with preservation of retinal layers within the ring (although there was some thinning of the outer photoreceptor layer), and loss of external limiting membrane and ellipsoid region, in addition to significant outer nuclear layer thinning in the macula outside the ring.⁶

In an SD OCT study of 7 patients with autoimmune retinopathy (6 of whom had either CAR or melanoma-associated retinopathy), Pepple et al¹¹ reported loss of the outer nuclear layer, external limiting membrane, and ellipsoid region (previously characterized as the inner segment–outer segment junction^{7,29}) in addition to cystic changes.^{7,11} Their study demonstrated progressive loss of outer retinal structure correlating with progressive visual field constriction in patients with CAR, with complete loss of outer nuclear layer beyond the outer border of the hyperautofluorescent ring.¹¹ Mesiwala et al¹² reported outer retinal changes detected by cross-sectional and en face SD OCT in a case of CAR resulting from Merkel cell carcinoma. They demonstrated correspondence between initial visual field loss and loss of photoreceptor reflectivity on en face SD OCT with marked progressive retinal atrophy seen on volumetric maps.¹² Likewise on SD OCT, our patient showed progressive degeneration of all of the outer retinal layers (decreased outer nuclear layer and photoreceptor layers, with loss of the outer limiting membrane and loss of the ellipsoid region) in the extrafoveal areas. He showed relative sparing of the foveal area with trace residual ellipsoid region remaining at his last visit.

To enable greater understanding of this rare disease, we performed serial AO imaging to assess for detectable in vivo changes in retinal structure with later comparison with histologic results. On AO imaging, cone photoreceptors were visible in a central elliptical area within the fovea, albeit at a decreased density compared with age-matched normal controls, which corresponded with the patient's preserved 3° central island of vision on GVF testing. A narrow band of hyporeflectivity containing sparse cones separated this central region from a surrounding annular area that contained both normal- and abnormal-appearing cones. Cone structure was extremely abnormal by $300 \mu\text{m}$, with large areas of hyporeflective cones interspersed with hyperreflective cones exhibiting irregular morphologic features. The surrounding retina was relatively hyporeflective with very few identifiable cones and clumps of hyperreflective material extending into the inner retina.

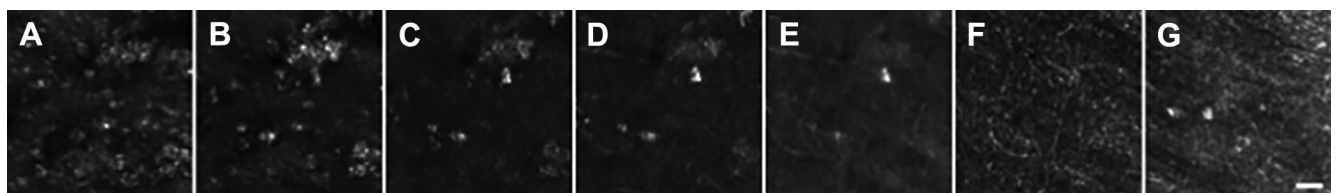


Figure 9. Through-focus images obtained at equal axial intervals extending from (A) the outer retina to (G) the surface of the nerve fiber layer. A, B, Outer retina shows clumping of hyperreflective material and is devoid of normal photoreceptor structure. C, D, E, Hyperreflective structures seen in the outer retina contain some material that appears to extend into the inner retina. F, G, Abnormal hyperreflective structures are also visible on the surface of the nerve fiber layer. Position on the retina of these through focus images is denoted by the white square on the adaptive optics montage in Figure 6B. Scale bar is $25 \mu\text{m}$.

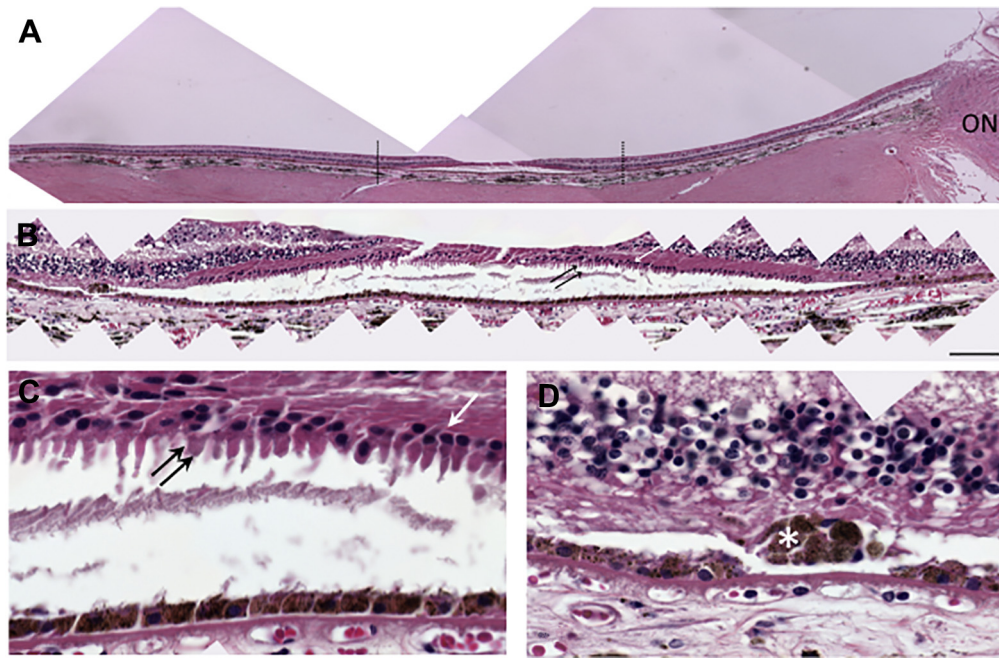


Figure 10. A, Low-power microphotograph montage of an 6- μm section through the center of the fovea stained with hematoxylin–eosin closely correlated to the position of the OCT scan noted in Figure 6. A portion of the optic nerve (ON) is seen on the right and the fovea is centered within the dashed lines. B, Higher-power microphotograph montage of the fovea between the dashed lines in (A) demonstrating relative sparing of the outer layers in this region (scale bar = 100 μm). C, Histopathologic sections revealing complete loss of photoreceptor cell nuclei except at the fovea, where a single layer of nuclei was seen in the outer nuclear layer (arrow) with attached cone inner segments (double arrow). D, Migrated retinal pigment epithelium cells and melanophages (asterisk) in the atrophic outer plexiform layer.

On histopathologic examination, migrated RPE cells and melanophages were seen in the atrophic inner nuclear layer correlating with the hyperreflective material seen on AO imaging. Although there are no prior reports of AO imaging in CAR, a study by Scoles et al³⁰ demonstrated presumably pathologic hyperreflective material in the inner retina in a variety of retinal disorders (including Leber congenital amaurosis, cone dystrophy, and Rubella retinopathy), leading to the hypothesis that the hyperreflective structures may reflect common mechanisms of retinal degeneration.

Adaptive optics imaging has been used to describe a variety of retinal disease processes, and previous work has correlated in vivo AO images of single cells to histologic results in animals.^{31–33} To date, AO has not been correlated with histopathologic analysis to validate its use in human disease. We present the first report using AO imaging in the disease CAR and the first report of in vivo AO imaging with histopathologic correlation in any disease. Our results provide histologic confirmation of the ability of AOSLO to identify cone photoreceptor loss in vivo in patients with retinal disease. As techniques continue to be refined and AO imaging gains more widespread clinical use, it undoubtedly will provide a useful means for detecting early changes in retinal disease and will provide a sensitive tool to monitor treatment response.

Acknowledgments. The authors thank our patient and his family, who graciously donated his eyes for scientific research;

Thurma McDaniel, for her expert technical skills; and Narsing Rao, MD, for help in processing the tissue and interpretation.

References

1. Adamus G, Ren G, Weleber RG. Autoantibodies against retinal proteins in paraneoplastic and autoimmune retinopathy. *BMC Ophthalmol.* 2004;4:4–5.
2. Ferreyra HA, Jayasundera T, Khan NW, et al. Management of autoimmune retinopathies with immunosuppression. *Arch Ophthalmol.* 2009;127:390–397.
3. Khan N, Huang JJ, Foster CS. Cancer associated retinopathy (CAR): an autoimmune-mediated paraneoplastic syndrome. *Semin Ophthalmol.* 2006;21:135–141.
4. Shildkrot Y, Sobrin L, Gragoudas ES. Cancer-associated retinopathy: update on pathogenesis and therapy. *Semin Ophthalmol.* 2011;26:321–328.
5. Adamus G. Autoantibody targets and their cancer relationship in the pathogenicity of paraneoplastic retinopathy. *Autoimmun Rev.* 2009;8:410–414.
6. Lima LH, Greenberg JP, Greenstein VC, et al. Hyperautofluorescent ring in autoimmune retinopathy. *Retina.* 2012;32:1385–1394.
7. Grewal DS, Fishman GA, Jampol LM. Autoimmune retinopathy and antiretinal antibodies: a review. *Retina.* 2014;34:827–845.
8. Braithwaite T, Vugler A, Tufail A. Autoimmune retinopathy. *Ophthalmologica.* 2012;228:131–142.
9. Adamus G, Guy J, Schmied JL, et al. Role of anti-recoverin autoantibodies in cancer-associated retinopathy. *Invest Ophthalmol Vis Sci.* 1993;34:2626–2633.

10. Sawyer RA, Selhorst JB, Zimmerman LE, Hoyt WF. Blindness caused by photoreceptor degeneration as a remote effect of cancer. *Am J Ophthalmol*. 1976;81:606–613.
11. Pepple KL, Cusick M, Jaffe GJ, Mruthyunjaya P. SD-OCT and autofluorescence characteristics of autoimmune retinopathy. *Br J Ophthalmol*. 2013;97:139–144.
12. Mesiwala NK, Shemonski N, Sandrian MG, et al. Retinal imaging with en face and cross-sectional optical coherence tomography delineates outer retinal changes in cancer-associated retinopathy secondary to Merkel cell carcinoma. *J Ophthalm Inflamm Infect*. 2015;5:53.
13. Lima LH, Cella W, Greenstein VC, et al. Structural assessment of hyperautofluorescent ring in patients with retinitis pigmentosa. *Retina*. 2009;29:1025–1031.
14. Roorda A, Duncan JL. Adaptive optics ophthalmoscopy. *Annu Rev Vis Sci*. 2015;1:19–50.
15. Dubra A, Sulai Y. Reflective afocal broadband adaptive optics scanning ophthalmoscope. *Biomedical Optics Express*. 2011;2:1757–1768.
16. Rossi EA, Rangel-Fonseca P, Parkins K, et al. In vivo imaging of retinal pigment epithelium cells in age related macular degeneration. *Biomedical Optics Express*. 2013;4:2527–2539.
17. Dubra A, Harvey Z. Registration of 2D images from fast scanning ophthalmic instruments. In: Fischer B, Dawant M, Lorenz C, eds. *Biomedical Image Registration*. Berlin, Heidelberg: Springer; 2010:60–71.
18. Li K, Roorda A. Automated identification of cone photoreceptors in adaptive optics retinal images. *J Opt Soc Am A Opt Image Sci Vis*. 2007;24:1358–1363.
19. Rossi EA, Roorda A. The relationship between visual resolution and cone spacing in the human fovea. *Nat Neurosci*. 2010;13:156–157.
20. Curcio C, Sloan K, Kalina RE, Hendrickson AE. Human photoreceptor topography. *J Comp Neurol*. 1990;292:497–523.
21. Song H, Chui TY, Zhong Z, et al. Variation of cone photoreceptor packing density with retinal eccentricity and age. *Invest Ophthalmol Vis Sci*. 2011;52:7376–7384.
22. Adamus G, Machnicki M, Elerding H, et al. Antibodies to recoverin induce apoptosis of photoreceptor and bipolar cells in vivo. *J Autoimmun*. 1998;11:523–533.
23. Adamus G, Machnicki M, Siegel GM. Apoptotic retinal cell death induced by autoantibodies of cancer-associated retinopathy. *Invest Ophthalmol Vis Sci*. 1997;38:283–291.
24. Adamus G, Yang S, Weleber RG. Unique epitopes for carbonic anhydrase II autoantibodies related to autoimmune retinopathy and cancer-associated retinopathy. *Exp Eye Res*. 2016;147:161–168.
25. Adamus G, Brown L, Schiffman J, Iannaccone A. Diversity in autoimmunity against retinal, neuronal and axonal antigens in acquired neuro-retinopathy. *J Ophthalm Inflamm Infect*. 2011;1:111–121.
26. Adamus G, Karren L. Autoimmunity against carbonic anhydrase II affects retinal cell functions in autoimmune retinopathy. *J Autoimmun*. 2009;32:133–139.
27. Wistrand PJ, Schenholm M, Lonnerholm G. Carbonic anhydrase isoenzymes CAI and CA II in the human eye. *Invest Ophthalmol Vis Sci*. 1986;27:419–428.
28. Adamus G, Aptsiauri N, Guy J, et al. The occurrence of serum autoantibodies against enolase in cancer-associated retinopathy. *Clin Immunol Immunopath*. 1996;78:120–129.
29. Spaide RF, Curcio CA. Anatomical correlates to the bands seen in the outer retina by optical coherence tomography: literature review and model. *Retina*. 2011;31:1609–1619.
30. Scoles D, Higgins BP, Cooper RF, et al. Microscopic inner retinal hyper-reflective phenotypes in retinal and neurologic disease. *Invest Ophthalmol Vis Sci*. 2014;55:4015–4029.
31. Geng Y, Dubra A, Yin L, et al. Adaptive optics retinal imaging in the living mouse eye. *Biomed Opt Express*. 2012;3:715–734.
32. Sharma R, Williams DR, Palczewska G, et al. Two-photon autofluorescence imaging reveals cellular structures throughout the retina of the living primate eye. *Invest Ophthalmol Vis Sci*. 2016;57:632–646.
33. Schallek J, Geng Y, Nguyen H, Williams DR. Morphology and topography of retinal pericytes in the living mouse retina using in vivo adaptive optics imaging and ex vivo characterization. *Invest Ophthalmol Vis Sci*. 2013;54:8237–8250.

Footnotes and Financial Disclosures

Originally received: May 12, 2017.

Final revision: June 6, 2017.

Accepted: June 13, 2017.

Available online: September 9, 2017. Manuscript no. ORET_2017_178.

¹ Flaum Eye Institute, University of Rochester Medical Center, Rochester, New York.

² Department of Ophthalmology, School of Medicine, University of Pittsburgh, Pittsburgh, Pennsylvania.

³ Department of Bioengineering, Swanson School of Engineering, University of Pittsburgh, Pittsburgh, Pennsylvania.

⁴ Center for Visual Science, University of Rochester, Rochester, New York.

Financial Disclosure(s):

The author(s) have made the following disclosure(s): E.A.R.: Patent — University of Rochester.

Supported by an unrestricted grant from Research to Prevent Blindness, Inc, New York, New York.

Author Contributions:

Conception and design: Williams, Rossi, DiLoreto

Analysis and interpretation: Williams, Rossi, DiLoreto

Data collection: Williams, Rossi, DiLoreto

Overall responsibility: Williams, Rossi, DiLoreto

Human Subjects: This study includes human subject/tissues. While alive the patient gave consent for publication of his clinical study and adaptive optics results. His family gave consent to for post-mortem analysis of his eyes and publication of any papers that resulted from this.

Abbreviations and Acronyms:

AO = adaptive optic; **AOSLO** = adaptive optics scanning laser ophthalmoscopy; **CAR** = cancer-associated retinopathy; **cSLO** = confocal scanning laser ophthalmoscopy; **FAF** = fundus autofluorescence; **GVF** = Goldmann visual field; **RPE** = retinal pigment epithelium; **SD** = spectral-domain.

Correspondence:

David A. DiLoreto, Jr., MD, PhD, Flaum Eye Institute, University of Rochester Medical Center, 601 Elmwood Avenue, Box 659, Rochester, NY 14610. E-mail: david_diloreto@urmc.rochester.edu.